

Pixel Characterization of a Protein-Based Retinal Implant Using a Microfabricated Sensor Array

Jordan A. Greco^{†,¶}, Luis André L. Fernandes[‡], Nicole L. Wagner[†],
Mehdi Azadmehr[‡], Philipp Häfliger[§], Erik A. Johannessen[‡] and Robert R. Birge^{†,||}

[†]*Department of Chemistry,
University of Connecticut, 55 North Eagleville Road, Storrs, CT 06269, USA*

[‡]*Department of Microsystems (IMS),
University College of Southeast Norway, Campus Vestfold,
Raveien 215, 3184 Borre, Norway*

[§]*Department of Informatics (IFI),
University of Oslo, P.O Box 1080 Blindern, 0316 OSLO, Norway*

[¶]*jordongreco9@gmail.com*
^{||}*rbirge@uconn.edu*

Received 5 October 2015
Accepted 4 April 2017

Retinal degenerative diseases are characterized by the loss of photoreceptor cells within the retina and affect 30-50 million people worldwide. Despite the availability of treatments that slow the progression of degeneration, affected patients will go blind. Thus, there is a significant need for a prosthetic that is capable of restoring functional vision for these patients. The protein-based retinal implant offers a high-resolution option for replacing the function of diseased photoreceptor cells by interfacing with the underlying retinal tissue, stimulating the remaining neural network, and transmitting this signal to the brain. The retinal implant uses the photoactive protein, bacteriorhodopsin, to generate an ion gradient in the subretinal space that is capable of activating the remaining bipolar and ganglion cells within the retina. Bacteriorhodopsin can also be photochemically driven to an active (**bR**) or inactive (**Q**) state, and we aim to exploit this photochemistry to mediate the activity of pixels within the retinal implant. In this study, we made use of a novel retinomorphoc foveated image sensor to characterize the formation of active and inactive pixels within a protein-based retinal implant, and have measured a significant difference between the output frequencies associated with the **bR** and **Q** states.

Keywords: protein-based retinal implants; foveated image sensors; bacteriorhodopsin; Q state; pixel mediation.

1. Introduction

Retinal degenerative diseases, including retinitis pigmentosa (RP) and age-related macular degeneration (AMD), involve the irreversible degeneration of the retinal photoreceptor cells.^{1,2} These diseases cause the layer of light sensing cells in the eye to degenerate over time, however, a significant portion of the underlying retinal tissue that transmits visual information to the brain remains largely intact.²⁻⁴ The resulting loss of

^{||}Corresponding author.

vision causes a significant decline in the quality of life for those affected. Retinitis pigmentosa, the most common of the inherited retinal degenerative disorders, affects approximately 1.5 million people worldwide and can affect people of all ages.^{5,6} Age-related macular degeneration is the leading cause of irreversible blindness among the elderly and is estimated to affect approximately 30 million people globally.^{7,8} There are currently no cures for patients with RP or AMD, and all available treatments only slow progression, are limited in effectiveness, and ultimately fail to prevent permanent loss of vision. Thus, there is a significant need for a therapy or prosthetic capable of restoring functional vision to RP and AMD patients.

Many new biotechnologies and treatments for blindness resulting from retinal degeneration have been developed during the past decade. While these treatments are still in their infancy and are limited by inherent drawbacks, a number of diverse approaches are currently under investigation in order to achieve a cure for diseases like RP and AMD. Novel and emerging approaches to treat retinal degeneration include stem cell tissue transplants,⁹⁻¹⁴ gene therapies,¹⁵⁻¹⁷ and optogenetic technologies.¹⁸⁻²⁴ Despite the promise of these treatments in design and preliminary efficacy, these biotechnologies are still under development and are now undergoing early clinical trials. Currently, intra-ocular and periocular injections and nutritional drug supplements are treatments which have shown success in slowing the progression of degeneration, however, limited efficacy is observed and the treated patient will eventually go blind.^{8,25,26} Electrode-based retinal implants, which currently represent the most common type of prosthetic used to restore vision, are being designed, developed, and commercialized in an effort to replace the function of the damaged photoreceptor cell layer within the retina. These retinal implants generally utilize an external apparatus to capture an image, convert that image into electrical signals, and stimulate the remaining neural circuitry within the degenerated retina. It has long been demonstrated that electrical stimuli can initiate the visual cascade when delivered in the extracellular domain of a retinal neuron.²⁷ Retinal implant architectures that exploit this electrical stimulation have seen some promise, and a number of companies and academic groups have demonstrated efficacy in the clinical setting, including efforts by Second Sight,²⁸⁻³⁰ Retinal Implant AG,³¹⁻³⁵ and the Epi-Ret 3 team.³⁶⁻³⁸

Of particular significance is the technology developed by Second Sight, which continues to be at the forefront of retinal prosthetic development and commercialization. The Argus II, created by Second Sight,²⁸⁻³⁰ was the first approved retinal prosthetic for clinical trials in both the US and Europe, and is currently the only approved implant on the market. The design of the electrode-based implant consists of a 60-electrode array placed in an epiretinal position. The Argus II has been implanted in over 100 patients with RP, and the patients were capable of detecting some motion and performing simple mobility tasks.³⁰ However, these retinal prosthetics have intrinsic shortcomings.³⁹ First, replicating the spatiotemporal patterns of the neurosensory network with electrode arrays is a challenge.⁴⁰ This problem is exacerbated by the low resolution associated with the electrode arrays, resulting in a limited ability to detect simple direction of motion through

high contrast, black and white gradients.^{28,41} Secondly, because the implant contains transscleral cables that penetrate the eye, the risk of infection is high and a number of serious adverse effects were observed in as many as 9 out of 30 patients, including conjunctival erosion, endophthalmitis, and hypotony.^{29,42} Furthermore, implantation requires laborious, complex surgery, and thereby limits adoption by the vitreoretinal surgeon community.^{39,43} According to lead researchers in the field, there is still a significant need for a device of higher resolution that also mitigates the risk of surgical complications.

The protein-based retinal implant offers unique solutions to the inherent shortcomings demonstrated in current electrode-based retinal prosthetics.⁴⁴ The retinal implant architecture is manufactured *via* a bottom-up approach and is comprised of multiple layers of the light-activated proton pump, bacteriorhodopsin (BR), oriented on a flexible, ion-permeable membrane *via* layer-by-layer (LBL) electrostatic adsorption.⁴⁵ The high resolution, subretinal implant converts light energy into an ion gradient that is capable of stimulating the remaining neural circuitry of the degenerated retina (Figure 1).⁴⁴ Like the electrode-based technologies, the protein-based prosthetic relies on the presence of the inner retinal tissue (i.e., intact bipolar and ganglion cells) in order to convert absorbed light energy into an electrochemical gradient that is interpreted by the brain as meaningful visual perception. The small and flexible protein-based retinal implant is a standalone prosthetic, which is capable of responding only to incident light without the influence of external devices that penetrate or communicate through the ocular tissue. The optical resolution of the implant is comparable to that of native photoreceptors due to the nanometer-scale features of the protein and the molecular packing of the biomaterials within the implant structure. Moreover, the unique photochemistry of the protein can be used to calibrate the retinal implant by modulating the active pixel area relative to the extent of retinal degeneration.⁴⁶

The protein-based retinal implant architecture harnesses the inherent pumping capability of BR, a feature necessary for the survival of the native organism, to generate a macroscopic ion gradient for retinal stimulation. Bacteriorhodopsin is a 26-kDa photoactive protein found in the outer membrane of the halophilic *archaeon*, *Halobacterium salinarum*.^{47,48} When the concentration of oxygen is insufficient to sustain growth *via* respiration (i.e., ATP generation by oxidative phosphorylation),^{47,48} BR is expressed within a two-dimensional crystalline lattice of trimers, known as the purple membrane.^{49,50} Upon the absorption of a photon by the protein-bound chromophore, all-*trans* retinal, BR transports a proton from the intracellular domain to the extracellular milieu *via* a series of transient photochemical intermediates, known as the photocycle (Figure 2).⁵¹ The net translocation of a proton generates a proton gradient, thereby driving cellular ATPase to synthesize ATP under anaerobic conditions.⁴⁷

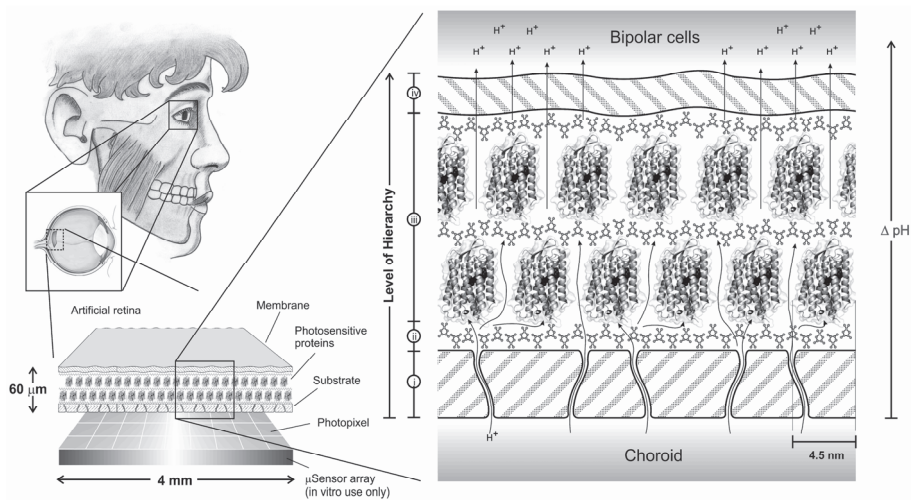


Figure 1. Architecture and application of the proposed protein-based retinal implant (or artificial retina). The implant acts as a subretinal implant located below the retinal tissue in place of degenerated photoreceptor cells. The implant consists of two ion-permeable membranes, depicted as (i) and (iv) in the RHS close up, with multilayers of the photosensitive protein, bacteriorhodopsin, contained between them. A polycation (ii) permits the deposition of alternating layers of the protein and polycation (iii) through a layer-by-layer electrostatic adsorption process. The orientation of the implant permits the generation of an H^+ gradient towards the remaining neural network of the retina. This novel approach of stimulating the intact bipolar cells mimics the native phototransduction cascade initiated by healthy photoreceptor cells. A photopixel microsensors array (bottom LHS image) was used in this study to examine the photoactive state of the bacteriorhodopsin *in vitro*, but is not a part of the prosthetic.

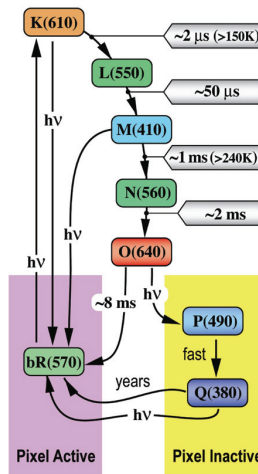


Figure 2. The main and branched photocycles of light adapted BR (**bR**). Upon the absorption of a single photon, the protein cycles through a series of transient intermediates (**K**, **L**, **M**, **N**, and **O**) and subsequently returns to the **bR** resting state. In order to access the branched photocycle (the **P** and **Q** states), a second photon must be absorbed to photochemically convert the **O** state to **P**. The resulting **Q** state is stable for several years at physiological temperature. The purple and yellow boxes also highlight the states in which the pixels within a retinal implant would be active or inactive, respectively. This figure is based on Figure 1 from Ref. 52.

The proton pumping mechanism initiated by the absorption of a photon by the retinal chromophore of BR is one of the most efficient photochemical reactions found in nature. The high quantum efficiency of this reaction (~65%) is identical to that of the visual pigment, rhodopsin, which is found in the photoreceptor cells of the human retina.^{53,54} Moreover, BR is a natural candidate for biophotonic devices due to a remarkable thermal stability and photochemical efficiency. Bacteriorhodopsin has a melting temperature in excess of 80 °C,⁵⁵ and has an observed photochemical cyclicality that exceeds 10⁶ photocycles before a 37% loss of the irradiated ensemble.⁵⁶⁻⁵⁸ Because BR is capable of withstanding high fluctuations in temperature, light flux, and chemical stress from a self-induced pH gradient, the biomaterial has been implemented as the photoactive medium in a number of devices for several decades.^{52,59}

Figure 2 provides a schematic of the BR photocycle and also highlights the ability of converting active pixels in a protein-based retinal implant to inactive pixels. This process is facilitated by accessing the branched photocycle (the **P** and **Q** states) *via* a sequential multiphoton process. The **Q** state, which was first described by Popp *et al.*,⁶⁰ contains a hydrolyzed 9-*cis* chromophore and differs from the other photointermediates within the BR photocycle because it is a thermally stable photoproduct that could last several years at ambient temperature.^{52,61} The **Q** state can be driven back to the resting (**bR**) state using high intensity UV light.⁶² Despite the observation of this photochemistry, access to the branched photocycle is highly inefficient for the native protein. Consequently, a significant research effort has been undertaken to use genetic engineering and directed evolution to identify enhanced mutants with efficient **Q** state formation.^{46,63} Over 10,000 mutants were screened during this study, and a number of mutants emerged with improved **Q** state performance, including the mutant V49A.⁴⁶ The enhanced BR biomaterial is capable of forming two stable and spectrally discrete photoproducts (**bR** and **Q**), which have been exploited as differentiable bits (bit 0 and bit 1) in protein-based volumetric memories and processors.^{52,64-66} Similarly, this photochemistry can provide a means to mediate pixels on the active surface area of a protein-based retinal implant. Because the **Q** state would prevent the protein from pumping protons, it has the potential to deactivate specific areas of the implant to prevent interference with functional photoreceptor cells following surgical implantation.

In this study, we seek to characterize the ability to mediate pixels within a protein-based retinal implant comprised of the high **Q**-forming mutant, V49A. Our approach makes use of a foveated complementary metal-oxide semiconductor (CMOS) imager, which is based on neural-inspired camera technologies that detect and process light similarly to the human eye. A foveated imager is a sensor that combines different pixel properties, which are dependent on their measured distance or computational delay relative to the center.⁶⁷ In using higher resolution in the center of the chip, one can simulate the fovea (higher concentration of cone photoreceptors) while keeping larger pixels towards the periphery of the chip working as large dynamic motion detectors (equivalent to the rods in the retina). Because we are not measuring the response to movement, we will focus on the properties of the static pixels only, leaving the use of the

larger dynamic peripheral pixels for future studies. The high resolution, sensitivity, and low noise properties of CMOS image sensors make them very good candidates for test platforms that can simulate the human retina and test the photosensitive properties of novel BR-based retinal implants.

Protein-based retinal implants were generated using the V49A BR mutant, and the implants were driven to the **Q** state by using LED-induced photochemistry. The hydrated retinal implants were then placed onto the foveated image sensor for relative light intensity measurements by the photodiodes, which is translated into an output frequency consisting of a series of action potentials (APs). At the conclusion of this study, we have shown that the image pixel properties can be extracted by attributing a light intensity to each of the pixels, which will allow for the differentiation between the **bR** or **Q** states and provide a basis for quantifying the extent to which the **Q** state has formed through a pixel light intensity map. The results of these proof-of-concept experiments show preliminary characterization of pixel mediation within a protein-based retinal implant, and ongoing experiments aim to quantify the limits of spatial resolution and generate the ability to drive local pixels between the two photoproducts.

2. Methods and Materials

2.1. Chemicals and buffers

All chemicals were purchased from Fisher Scientific, Inc. (Pittsburg, PA) or Sigma Aldrich (St. Louis, MO). Because an alkaline pH is necessary to produce and isolate the **Q** photoproduct, a 50 mM glycine buffer at pH 9.5 was prepared and used for all solution-based experiments in this study.⁴⁶

2.2. Strain generation, protein isolation, and purification

The high **Q**-forming mutant, V49A, was first identified using Type I directed evolution.⁴⁶ In order to express this mutant form of BR, mutant DNA was transformed into the MPK409 cell line of *H. salinarum* using methods outlined by Peck *et al.*⁶⁸ Purple membrane fractions were then prepared and isolated according to standard procedures.^{69,70}

2.3. Manufacturing of the protein-based retinal implants

The protein-based retinal implants were comprised of a multilayered, BR-based thin film generated *via* sequential electrostatic adsorption, which was achieved through a LBL manufacturing technique.^{45,71,72} The multilayered thin films are capable of harnessing and amplifying the proton pumping action of BR if the protein is uniformly oriented in the film at an optimal optical density. There must be enough layers of BR to adequately absorb incident light while also generating an appreciable unidirectional ion gradient for retinal stimulation. The solid support surface of the thin film is a bioinert, ion-permeable mesh comprised of polyethylene terephthalate (PET) microfibers. This material has previously found success for use in the eye^{73,74} and is amenable to surface modification in

order to serve as a scaffolding for multilayers of BR within our protein-based retinal implant. Because the LBL process requires a charged surface for subsequent electrostatic adsorption, the PET film was first exposed to conditions that facilitate the reduction of surface carbonyl functional groups that renders the surface negatively charged.⁷⁵⁻⁷⁷

Following preparation of the PET scaffolding, the LBL manufacturing technique was implemented as first described by He *et al.*^{45,71,72} In brief, the PET film is first dipped in a solution of poly(diallyldimethyl ammonium chloride), followed by rinse periods in ddH₂O (Millipore, Billerica, MA) and a short drying interval. The thin film is then transferred to a solution of BR and rinsed twice in basic glycine buffer. It is important to note that this technique was carried out so that only one surface of the film was coated during the LBL methods outlined above.

2.4. Preparation of the Q state

The bacteriorhodopsin mutant used in this study (V49A) was selected due to the identification of this protein as a high Q-forming mutant.⁴⁶ The Q photoproduct was formed while the protein was contained within the multilayered thin film. The thin films were placed in a petri dish filled with enough glycine buffer (50 mM; pH 9.5) to completely hydrate the film for the duration of the illumination period. The film was placed under an LED light bank (100 mW/cm²), which contained 12 red (>640 nm) Luxeon III Lambertian LEDs that were each driven at 850 mA, for 8 hours at ambient temperature. Prior to further experiments, the Q state thin film was hydrated within the buffered solution and the petri dish was wrapped in aluminum foil to prevent exposure to ambient light.

2.5. Absorption spectroscopy

All absorption spectra were collected at ambient temperature using a Varian Cary 5000 UV-visible spectrophotometer (Palo Alta, CA). The retinal implants were inserted into a 1 mm quartz spectrophotometer cell (Starna Cells, Inc.; Atascadero, CA) and the films were suspended in 50 mM glycine buffer (pH 9.5). A bare PET mesh film in buffer was used as the blank for all measurements.

2.6. Foveated image sensors

Modern CMOS sensor-based cameras offer an excellent optical resolution.⁷⁸ The CMOS image sensors that form the core of these cameras benefit from technology scaling that has provided them with a resolution increase (pixel size reduction) combined with the possibility to include more on-chip image processing circuitry. However, size scaling beyond sub-micron (< 0.25 μ m) processing technologies is limited by dark current noises, tunneling effects through thin gate oxides, and a low photoresponsivity due to a combination of shallow junctions and high doping.⁷⁹ Continuous effort is seeking to negotiate these limiting parameters through a gradual improvement of the fabrication technologies used, which together with the low cost of manufacture have continued to

secure the commercial success of CMOS image sensors. This has, in turn, paved the way for new application possibilities, such as neural-inspired or retinomorphic cameras,^{80,81} that mimic the way human eye detects and processes light and images.

The foveated image sensor used in this project was created using the commercial 0.35 μm CMOS processing technology, which measures $3.15 \times 3.15 \text{ mm}^2$ in extent.⁶⁷ Like most neural-inspired circuits, this camera communicates with voltage pulses that resemble APs. Each pixel consists of a photodiode and the associated processing circuitry. The circuitry of the static photopixel cells (located in the center of the image sensor) consists mainly of an integrator. It integrates a current linearly proportional to the light level over a short period of time, and when a threshold is reached, an AP is fired. The AP is conveyed off-chip by peripheral logic and the pixel is reset (Figure 3). Thus, the firing frequency reflects the light intensity collected by this pixel.

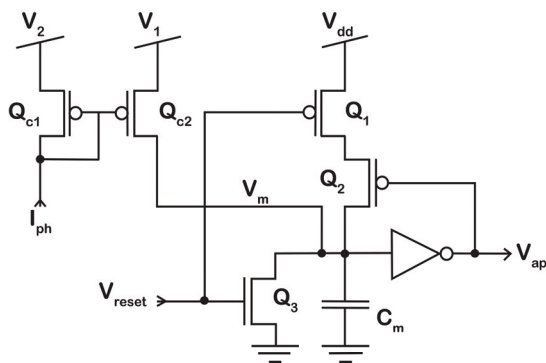


Figure 3. Foveated imager pixel logic. The photodiode is connected to I_{ph} and the current is mirrored in Q_{c1} - Q_{c2} , which can also act as an amplifier (tilted current mirror), charging C_m . Once V_m has reached the inverter threshold, it spikes an AP (V_{ap}) and initiates the communication circuit. Q_2 opens, and since V_{reset} is active high, Q_1 is already open and V_m is pulled to V_{dd} . When the communication circuit sends a reset signal to the pixel, V_m is set to ground and the reset signal goes low again, charging C_m once more.

In more detail, the photo current i conveyed by the current mirror charges a capacitor C_m and, when the voltage across it reaches the threshold of the inverter, the output from the inverter changes from state 1 to 0 (digital representation). Through a feedback loop, the transistor Q_2 is activated and capacitor C_m is stabilized at the potential V_{dd} when the reset signal is low. When the reset signal is asserted, the transistor Q_1 will deactivate, and C_m will empty its charge to ground through Q_3 , reaching the initial state. The size of C_m is essential to determine how fast the threshold voltage of the inverter will be reached. The voltage at C_m (V_m) is given by Eq. (1):

$$V(t)_m = \frac{1}{C} \int_0^t i d\tau + V(0). \tag{1}$$

For $V(0) = 0$:

$$V(t)_m = \frac{1}{C} \int_0^t id\tau. \quad (2)$$

From Eq. (2), it is clear that the use of a small capacitor (capacitance, C) will reach the threshold potential ($V(t)_m$) faster. This also comes at the cost of a noisier circuit in which the leakage current (dark current at zero light intensity) charges a smaller capacitor faster, resulting in the generation of APs. In contrast, a larger capacitor will take a longer time to charge under these conditions, thus decreasing the rate of APs and, consequently, the noise. This makes it less dependent on the dark current, but is at the cost of operating as a slower circuit. The area of the capacitor used in the static pixels of the foveated image sensor, $C_m = 2.48 \times 10^{-4} \mu\text{m}^2$, corresponds to a capacitance of 221.58 fF. The dark current will charge this capacitor at a rate that corresponds to the generation of 1 AP/s at zero lux. Increasing the light level to 3 lux (comparable to the test conditions described below) increases the firing rate to 8 AP/s. Hence, a change in the photocycle state of BR will reflect a change in light intensity and, consequently, a shift in the AP frequency.

The dynamic photopixel cells that are located in the periphery of the chip fire an AP if changes in light are detected according to the photoreceptor circuit described by Delbrück & Mead,⁸² where an electronic photoreceptor outputs a voltage that is logarithmic to the light intensity. The dynamic pixels are adaptive to various light levels and the APs are fired as the speed of that adaptation exceeds a certain threshold.⁶⁷ The photodiodes in all of the pixels are made from substrate diodes (n-well regions defined by, e.g., boron doping) in the bulk p- substrate of the chip.

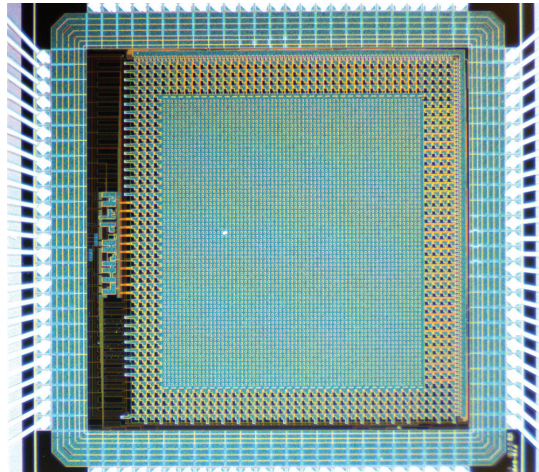


Figure 4. Photomicrograph of the foveated image sensor. Four rows of dynamic pixels (616 total pixels) surround the central 76 x 67 array of static pixels.

While still large when compared to commercial CMOS image sensor pixels due to the in-pixel logic, the static photopixels are smaller than the dynamic pixels in order to produce high resolution pictures, measuring $26.8 \times 25.2 \mu\text{m}^2$ with a fill factor (photo-diode area) of 11.3 %. The dynamic pixels are larger, measuring $53.6 \times 50.4 \mu\text{m}^2$, with a fill factor of 50.4 %. The photodiodes for the dynamic pixels are larger in order to achieve a higher sensitivity to light intensity variations. The pixel array is made up of 76×67 static cells in the center surrounded by 616 dynamic pixels according to (Figure 4).

2.6.1. AER communication protocol

The schematic in Figure 3 (except for the current mirror) is called an Integrate and Fire circuit and is a good example of a mixed-mode circuit. It is based on the “self-reset neuron”.⁸³ A real biological neural network, which consists of point-to-point connections, is difficult to implement on an artificial neural CMOS chip due to a limiting amount of metal layers that are available for routing combined with a limited amount of contact pads that are available for interconnecting the generated signals to an external circuitry. A solution for asynchronous neuromorphic communication is the Address Event Representation (AER) protocol.⁸⁴ Most neurons communicate by way of nerve pulses or APs *via* dedicated point-to-point connections (axons). This is in contrast to the communication channels between computers, or inside computers, that transmit more complex signals at higher rates than an axon. The physical channels are mostly shared and time multiplexed by several components keeping a lower density. As neuromorphic engineers try to implement systems that are organized more like the nervous system, communicating internal signals like the brain can become a major obstacle to electronics. The human brain contains about 10^{11} neurons, each of which has 1,000 to 10,000 synapses. All of those synapses receive input *via* a dedicated output line of the sending neuron, making the brain densely packed with connections between cortical areas and other parts.

Since neurons/pixels use APs to communicate, the AER bus is used to send the address of the neuron/pixel off-chip, either to a receiving neuromorphic circuit or a computer where the activity can be visualized, e.g., as a gray scale image of average pixel activity. This communication protocol takes advantage of the speed in integrated circuits, compensating for the lack of connections. The functioning principle can be explained as follows. When a neuron wishes to send an AP, it places its address on a digital bus *via* an encoder. Synapses that are supposed to receive that AP are connected to the same bus *via* a decoder and get stimulated when their address occurs (Figure 5). The bus can only transmit APs serially but does it much faster than an axon. It can transmit APs so tightly spaced in time that, for a network of neurons that operate on a natural time scale, these pulses are virtually instantaneous. Since multiple point-to-point connections share the same bus, it is necessary to have a bus control mechanism for handling collisions. The AER communication protocol is described in detail in Ref. 67.

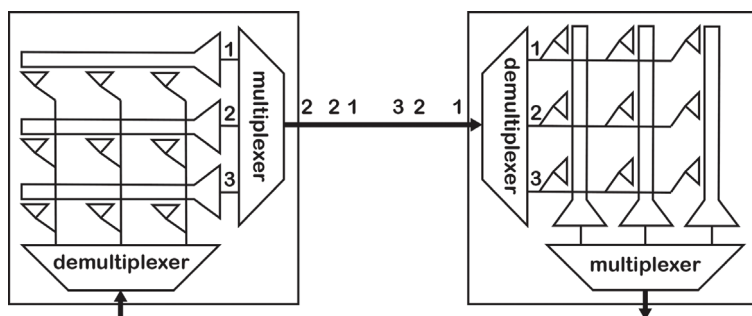


Figure 5. Schematic of the Address Event Representation (AER) principle.

2.7. *Q* state detection

In order to characterize the pixel content contained within the protein-based retinal implant, each film was placed directly on top of the foveated image sensor with a particular emphasis on the static pixels within the photodiode array. The retinal implants were either in the **BR** resting state or driven to the **Q** state using the photonic criteria described above.⁴⁶ Each film was placed in a consistent orientation on the chip so that the pixel intensity measurements were under identical conditions. The sensor array was embedded in a sensor housing that protected the electrical interconnections from the hydrated films. Silicone purchased from Dow Corning (3140 RTV coating, Midland, MI) was used to encapsulate the wire bonded contact pads on the sensor array. Once the BR-based retinal implant film was placed directly on the foveated imager (Figure 1, bottom LHS), the number of spikes generated by each pixel was measured under a controlled illumination environment (approximately 3 lux) for a 1-minute duration. The foveated image sensor does not provide colorimetric images, and therefore, a gray scale analysis of the pixels was used to measure the contrast between the two photoproducts of interest. The measured output is equivalent to the pulse frequencies that are proportional to the light intensities monitored by each pixel within the foveated imager.

3. Results and Discussion

3.1. *Q* state formation

The absorption spectra of the implants were first measured to demonstrate the ability to convert the V49A layers between the two photoproducts (**BR** and **Q** states, Figure 6). The solid line (1) shows the absorption spectra of the implant in the **BR** state, whereas the dashed line (2) shows the absorption spectra of the implant in the **Q** state. A photograph of the films with the V49A protein in each photostate is shown in the insert. The **Q** state has a transparent/yellow color with an absorption maximum on the periphery of the visible spectrum (~380 nm). This state is reversible, but a high intensity UV light is required to drive the protein back to the photoactive **BR** state, which is characterized by

the vibrant, purple color shown in Figure 6 and has an absorption maximum of 570 nm. Spectral analysis indicates that the film has completely converted from the **bR** resting state to the **Q** state using the red LED light bank (100 mW/cm^2) for 8 hours. There is no spectroscopic evidence of protein denaturation following the immobilization of the protein within the retinal implant architecture, and following the intense red light exposure, the device retained a high optical clarity as suggested by minimal absorption in a wavelength range of $>700 \text{ nm}$.

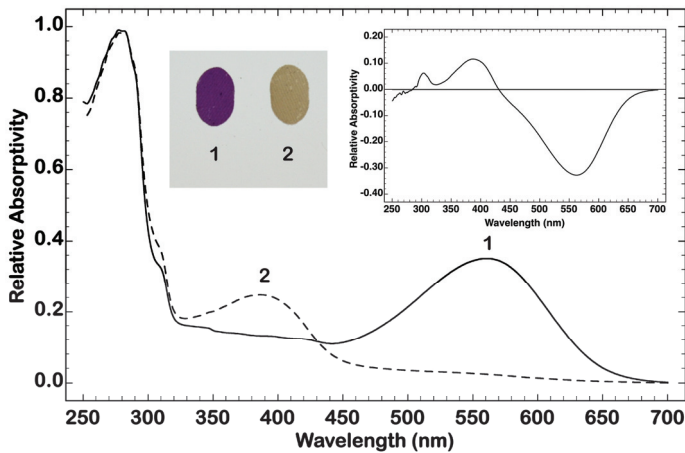


Figure 6. Absorption spectra of the protein-based retinal implants in the **bR** state (solid line) and the **Q** state (dashed line). The left inset image is a photograph of the retinal implants in the **bR** state (1) and **Q** state (2) after red LED illumination. The right inset figure shows the difference spectra, in which the **bR** state spectrum is subtracted from the **Q** state spectrum.

3.2. Pixel characterization using a foveated image sensor

The foveated image sensor was used as a proof-of-concept experiment to demonstrate the capability of monitoring **Q** state formation within a retinal implant architecture. Following a demonstration that the retinal implant could be completely converted to the **Q** photoproduct under intense LED illumination (Figure 6), the image sensor was subsequently used to quantify differences in pixel intensities through a contrast comparison between the **bR** and **Q** states. Because the foveated imager does not provide a color image, a gray scale was used to measure the difference between the purple pixels of **bR** and the transparent/yellow pixels of the **Q** state. A histogram of the image acquired by the foveated image sensor (Figures 7A and 7B), shows a shift in the pixel intensity to the right, reflecting an increase in the number of AP firing events recorded by the pixels (x-axis). The number of active pixels corresponding to the image area that is illuminated is depicted on the y-axis. The observed shift corresponds to the formation of the **Q** state where a brighter image will result in a higher number of APs. In contrast, a "zero" events situation would correspond to the reference background (black color) where no image is

detectable, and where only the dark current noise would prevail. This result is expected, since a brighter shade of gray results in a higher light intensity which in turn triggers the photodiodes to generate more APs over a given time domain. Because the **bR** state results in a darker shade of gray, the light intensity falls and the photodiodes would reduce the number of APs generated over the same period. However, a comparable amount of active photodiodes should be present in both the **bR** and **Q** state recording.

Throughout this study, we first recorded the maximum frequency corresponding to complete **Q** state formation, and the lowest frequency, corresponding to the film resting in the **bR** state. Considering Figure 7, there is an output frequency increase of 2 AP/s (or 120 AP/min) in forming the **Q** state. The inset images for Figures 7A and 7B shows the measured pixel intensity distribution map for the retinal implant in both the **bR** and **Q** states, respectively (as the film is placed onto the static pixels of the foveated imager). Note that the curved edges of the retinal implant can be observed in the top right hand corner of each of the inset images, and that the implant was placed in an identical location on the foveated imager between measurements of the **bR** and **Q** states. This placement was performed to ensure that the ambient light conditions and relative pixel measurements were consistent throughout the study. The measured pixel intensities were taken from the same location on the imager for both states, which is shown by the white boxes of the inset images in Figure 7.

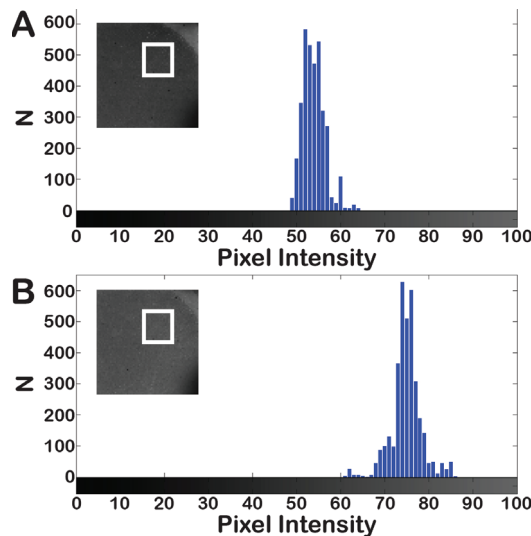


Figure 7. Quantification of pixel intensity of BR in the **bR** state (A) and the **Q** state (B). The value, N , on the y-axis was measured by the static pixels on the foveated image sensor as the number of events recorded during a 1 minute time period at each pixel intensity. The x-axis provides a graded gray scale used to measure pixel intensities of the retinal implant for each state. The inset images show the retinal implants in gray scale and the corresponding areas of measurement given by the white squares. There is a light intensity variation between each of the photostates of approximately 25%, or 0.85 lux, which translates to 2 AP/s according to Ref. 67.

The pixel intensity analysis demonstrates that there is a significant frequency separation observed between the two accessible photoproducts of the retinal implant based on the V49A BR mutant, and that the protein was uniformly present in each respective photostate within the sensitivity of the imager. This result also mirrors the spectral analysis shown in Figure 6, in which the protein contained within the retinal implant was shown to completely convert from the **bR** resting state to the **Q** state. While this study does not approach the measurability limits of the foveated image sensor in terms of resolution, sensitivity, and function (i.e., dynamic vs. static pixels), the first steps have been taken towards monitoring two spectrally distinct photoproducts within a multilayered thin film architecture, and have laid the groundwork for future experiments that will further characterize the pixel mediation properties of BR-based retinal implants.

Following these initial proof-of-concept experiments, there are a number of conditions that remain to be optimized for further pixel characterization of the retinal prosthetic. First, the ambient light conditions that were used for measurement should be modulated to promote the greatest output frequency separation between the **bR** and **Q** states. We have so far used ambient laboratory lighting for these measurements, but the use of monochromatic light sources will lead to enhanced performance of the sensor and more controlled contrast and resolution. Once the data collection conditions are optimized to discriminate between frequency bands of firing APs, intermediate frequencies should be measured during the **Q** state formation process in order to monitor incomplete conversion and, perhaps, the kinetics of formation within the retinal implant architecture. Finally, we would like to develop a more sensitive irradiation technique based on fiber optics to locally drive individual pixels or pixel clusters within the retinal implant to the **Q** state. Our global analysis has so far predicted that the foveated imager is capable of differentiating between **bR** and **Q**, however, we hope to further exploit the sensitivity of the CMOS sensor to quantify the limits of pixel mediation within our retinal implant.

4. Conclusion

This work demonstrated the feasibility of using CMOS image sensors, in this case a foveated image sensor, as a microsensor array platform for testing the light sensitivity of two stable photoproducts within a novel photosensitive protein-based retinal implant. The foveated imager measured a significant difference of output frequencies between the **bR** and **Q** states using gray scale analysis. This result also mirrored the spectral properties of the two isolatable photoproducts of BR. Moreover, this investigation represents a first example that demonstrates the possibility of not only fabricating a protein-based retinal implant using a BR mutant, but also to characterize the photoactive behavior of BR that will be responsible for restoring vision at a resolution that is only limited by the density of the protein layers. The **bR** and **Q** states of the high **Q**-forming BR mutant, V49A, provide a photochemical pathway towards pixel mediation within the retinal implant, which will help RP or AMD patients manage the gradual progression of retinal degeneration. Areas of the retina with high retinal degeneration will be targeted with active pixels in the **bR** state, where light-activated proton pumping can be harnessed for

retinal stimulation. Deactivation of pixels *via* the accession of **Q** will prevent interference with functional patches of photoreceptor cells. We envision that pixels could be selectively driven to the **Q** state following implantation of the retinal prosthetic using a targeted, multiphoton optical apparatus.

The experiments performed here are the first step in a series of ongoing work to explore the ability to mediate pixels of the BR-based retinal implant, quantify the spatial resolution, and develop the optics necessary for localized **Q** state formation within the retinal implant. In addition to optimizing the experimental conditions for the studies outlined above, we are assembling an optical system for irradiation of areas identical to the size of one pixel of the foveated image sensor to validate the ability of modulating the surface area on a scale relevant to *in vivo* pixel mediation. Finally, we are currently developing a similar microsensor array platform using ion-sensitive field-effect transistors (ISFETs) for the on-chip measurement of the proton-pumping action of BR as a means to quantify spatial sensitivity of the protein-based retinal implant.

Acknowledgement

Work conducted in the laboratory of R.R.B. was supported by grants from the National Institutes of Health (GM-34548, 1R41 EY023461), the National Science Foundation (EMT-0829916, IIP-144822, IIP-1542456), and the Harold S. Schwenk Sr. Distinguished Chair in Chemistry. Researcher L.A.L.F. was funded by the Research Council of Norway under the Leiv Eriksson mobility program (234703/F11). Work in the laboratory of E.A.J. was supported by the Oslofjord Fund (239124).

References

1. D. T. Hartong, E. L. Berson and T. P. Dryja, Retinitis pigmentosa, *Lancet*, **368**, 18-24 (2006).
2. K. M. Gehrs, J. R. Jackson, E. N. Brown, R. Allikmets and G. S. Hageman, Complement, age-related macular degeneration and a vision of the future, *Arch. Ophthalmol.*, **128**, 349-358 (2010).
3. A. Santos, M. S. Humayun, E. de Juan, R. J. Greenburg, M. J. Marsh, I. B. Klock and A. H. Milam, Preservation of the inner retina in retinitis pigmentosa. A morphometric analysis, *Arch. Ophthalmol.*, **115**, 511-515 (1997).
4. J. L. Stone, W. E. Barlow, M. S. Humayun, E. J. de Juan and A. H. Milam, Morphometric analysis of macular photoreceptors and ganglion cells in retinas with retinitis pigmentosa, *Arch. Ophthalmol.*, **110**, 1634-1639 (1992).
5. E. L. Berson, Retinitis pigmentosa: Unfolding its mystery, *Proc. Natl. Acad. Sci. U.S.A.*, **93**, 4526-4528 (1996).
6. R. G. Weleber, Inherited and orphan retinal diseases: Phenotypes, genotypes, and probable treatment groups, *Retina*, **25**, S4-S7 (2005).
7. D. S. Friedman, B. J. O'Colmain, B. Munoz, S. C. Tomany, C. McCarty, P. T. de Jong, B. Nemesure, P. Mitchell and J. Kempen, Prevalence of age-related macular degeneration in the United States, *Arch. Ophthalmol.*, **122**, 564-572 (2004).
8. J. P. Hubschman, S. Reddy and S. D. Schwartz, Age-related macular degeneration: Current treatments, *Clin. Ophthalmol.*, **3**, 155-166 (2009).

9. L. A. Wiley, E. R. Burnight, A. E. Songstad, A. V. Drack, R. F. Mullins, E. M. Stone and B. A. Tucker, Patient-specific induced pluripotent stem cells (iPSCs) for the study and treatment of retinal degenerative diseases, *Prog. Retinal Eye Res.*, **44**, 15-35 (2015).
10. P. Y. Baranov, B. A. Tucker and M. J. Young, Low-oxygen culture conditions extend the multipotent properties of human retinal progenitor cells, *Tissue Eng., Part A*, **20**, 1465-1475 (2014).
11. W. Chato, M. Abdouh, R.-H. Duparc and G. Bernier, Bmi1 distinguishes immature retinal progenitor/stem cells from the main progenitor cell population and is required for normal retinal development, *Stem Cells*, **28**, 1412-1423 (2010).
12. B. P. Hafler, N. Surzenko, K. T. Beier, C. Punzo, J. M. Trimarchi, J. H. Kong and C. L. Cepko, Transcription factor *Olig2* defines subpopulations of retinal progenitor cells biased towards specific cell fates, *Proc. Natl. Acad. Sci. U. S. A.*, **109**, 7882-7887 (2012).
13. J. Luo, P. Y. Baranov, S. Patel, H. Ouyang, J. Quach, F. Wu, A. Qiu, H. Luo, C. Hicks, J. Zeng, J. Zhu, J. Lu, N. Sfeir, C. Wen, M. Zhang, V. Reade, S. Patel, J. Sinden, X. Sun, P. Shaw, M. J. Young and K. Zhang, Human retinal progenitor cell transplantation preserves vision, *J. Biol. Chem.*, **289**, 6362-6371 (2014).
14. S. Schmitt, U. Aftab, C. Jiang, S. Redenti, H. Klassen, E. Miljan, J. Sinden and M. Young, Molecular characterization of human retinal progenitor cells, *Invest. Ophthalmol. Vis. Sci.*, **50**, 5901-5908 (2009).
15. A. Gonzalez-Cordero, E. L. West, R. A. Pearson, Y. Duran, L. S. Carvalho, C. J. Chu, A. Naeem, S. J. Blackford, A. Georgiadis, J. Lakowski, M. Hubank, A. J. Smith, J. W. Bainbridge, J. C. Sowden and R. R. Ali, Photoreceptor precursors derived from three-dimensional embryonic stem cell cultures integrate and mature within an adult degenerate retina, *Nat. Biotechnol.*, **31**, 741-747 (2013).
16. S. D. Schwartz, J. P. Hubschman, G. Heilwell, V. Franco-Cardenas, C. K. Pan, R. M. Ostrick, E. Mickunas, R. Gay, I. Klimanskaya and R. Lanza, Embryonic stem cell trials for macular degeneration: A preliminary report, *Lancet*, **379**, 713-720 (2012).
17. A. O. Cramer and R. E. MacLaren, Clinical trials using induced pluripotent stem cells from bench to bedside: Application to retinal diseases, *Curr. Gene Ther.*, **13**, 139-151 (2013).
18. L. Buchen, Neuroscience: Illuminating the brain, *Nature*, **465**, 26-28 (2010).
19. E. S. Boyden, F. Zhang, E. Bamberg, G. Nagel and K. Deisseroth, Millisecond-timescale, genetically targeted optical control of neural activity, *Nat. Neurosci.*, **8**, 1263-1268 (2005).
20. X. Han and E. S. Boyden, Multiple-color optical activation, silencing, and desynchronization of neural activity, with single-spike temporal resolution, *PLoS One*, **2**, e299 (2007).
21. V. Busskamp and B. Roska, Optogenetic approaches to restoring visual function in retinitis pigmentosa, *Curr. Opin. Neurobiol.*, **21**, 942-946 (2011).
22. V. Busskamp, S. Picaud, J. A. Sahel and B. Roska, Optogenetic therapy for retinitis pigmentosa, *Gene Ther.*, **19**, 1-7 (2011).
23. P. Degenaar, N. Grossman, M. A. Memon, J. Burrone, M. Dawson, E. Drakakis, M. Neil and K. Nikolic, Optobionic vision – a new genetically enhanced light on retinal prosthesis, *J. Neural. Eng.*, **6** (2009).
24. J. Cehajic-Kapetanovic, C. Eleftheriou, A. E. Allen, N. Milosavljevic, A. Pienaar, R. Bedford, K. E. Davis, P. N. Bishop and R. J. Lucas, Restoration of vision with ectopic expression of human rod opsin, *Curr. Biol.*, **25**, 2111-2122 (2015).
25. K. Shintani, D. L. Shechtman and A. S. Gurwood, Review and update: Current treatment trends for patients with retinitis pigmentosa, *J. Am. Optom. Assoc.*, **80**, 384-401 (2009).
26. J. L. Kovach, S. G. Schwartz, H. W. Flynn Jr. and I. U. Scott, Anti-VEGF treatment strategies for wet AMD, *J. Ophthalmol.*, **2012** (2012).
27. W. M. Grill and J. T. Mortimer, Stimulus waveforms for selective neural stimulation, *IEEE Eng. Med. Biol. Mag.*, **14**, 375-385 (1995).

28. J. D. Weiland, A. K. Cho and M. S. Humayun, Retinal prostheses: Current clinical results and future needs, *Ophthalmology*, **118**, 2227-2237 (2011).
29. M. S. Humayun, J. D. Dorn, L. da Cruz, G. Dagnelie, J.-A. Sahel, P. E. Stanga, A. V. Cideciyan, J. L. Duncan, D. Elliott, E. Filley, A. C. Ho, A. Santos, A. B. Safran, A. Arditì, L. B. Del Priore and R. J. Greenberg, Interim results from the international trial of Second Sight's visual prosthesis, *Ophthalmology*, **119**, 779-788 (2012).
30. M. P. Barry and G. Dagnelie, Use of the Argus II retinal prosthesis to improve visual guidance of fine hand movements, *Invest. Ophthalmol. Vis. Sci.*, **53**, 5095-5101 (2012).
31. R. Wilke, V.-P. Gabel, H. Sachs, K.-U. Bartz-Schmidt, F. Gekeler, D. Besch, P. Szurman, A. Stett, B. Wilhelm, T. Peters, A. Harscher, U. Grepmaier, S. Kibbel, H. Benhav, A. Bruckmann, K. Stingl, A. Kusnyerik and E. Zrenner, Spatial resolution and perception of patterns mediated by a subretinal 16-electrode array in patients blinded by hereditary retinal dystrophies, *Invest. Ophthalmol. Vis. Sci.*, **52**, 5995-6003 (2011).
32. H. Benav, K. U. Bartz Schmidt, D. Besch, A. Bruckmann, F. Gekeler, U. Grepmaier, A. Harscher, S. Kibbel, A. Kusnyerik, T. Peters, H. Sachs, A. Stett, K. Stingl, B. Wilhelm, R. Wilke, W. Wrobel and E. Zrenner, Restoration of useful vision up to letter recognition capabilities using subretinal microphotodiodes, *Conf. Proc. IEEE Eng. Med. Biol. Soc.*, **2010**, 5919-5922 (2010).
33. A. Kusnyerik, U. Grepmaier, R. Wilke, F. Gekeler, B. Wilhelm, H. Sachs, K. U. Bartz-Schmidt, U. Klöse, K. Stingl, M. D. Resch, A. Hekmat, A. Bruckmann, K. Karacs, J. Nemeth, I. Suveges and E. Zrenner, Positioning of electronic subretinal implants in blind retinitis pigmentosa patients through multimodal assessment of retinal structures, *Invest. Ophthalmol. Vis. Sci.*, **53**, 3748-3755 (2012).
34. K. Stingl, K. U. Bartz-Schmidt, D. Besch, A. Braun, A. Bruckmann, F. Gekeler, U. Grepmaier, S. Hipp, G. Hortdorfer, C. Kernstock, A. Koitschev, A. Kusnyerik, H. G. Sachs, A. Schatz, K. T. Stingl, T. Peters, B. Wilhelm and E. Zrenner, Artificial vision with wirelessly powered subretinal electronic implant alpha-IMS, *Proc. R. Soc. B*, **280**, 20130077 (2013).
35. E. Zrenner, Fighting blindness with microelectronics, *Sci. Transl. Med.*, **5**, 210-216 (2013).
36. S. Klauke, M. Goertz, S. Rein, D. Hoehl, U. Thomas, R. Eckhorn, F. Bremmer and T. Wachtler, Stimulation with a wireless intraocular epiretinal implant elicits visual percepts in blind humans, *Invest. Ophthalmol. Vis. Sci.*, **52**, 449-455 (2011).
37. G. Roessler, T. Laube, C. Brockmann, T. Kirschkamp, B. Mazinani, M. Goertz, C. Koch, I. Krisch, B. Sellhaus, H. Khiem Trieu, J. Weis, N. Bornfeld, H. Röhgen, A. Messner, W. Mokwa and P. Walter, Implantation and explanation of a wireless epiretinal retina implant device: Observations during the EPIRET3 prospective clinical trial, *Invest. Ophthalmol. Vis. Sci.*, **50**, 3003-3008 (2009).
38. J. Menzel-Severing, T. Laube, C. Brockmann, N. Bornfeld, W. Mokwa, B. Mazinani, P. Walter and G. Roessler, Implantation and explanation of an active epiretinal visual prosthesis: 2-year follow-up data from the EPIRET3 prospective clinical trial, *Eye*, **26**, 501-509 (2012).
39. M. Javaheri, D. S. Hahn, R. R. Laxhanpal, J. D. Weiland and M. S. Humayun, Retinal prostheses for the blind, *Ann. Acad. Med. Singapore*, **35**, 137-144 (2006).
40. D. Palanker, A. Vankov, P. Huie and S. Baccus, Design of a high-resolution optoelectronic retinal prosthesis, *J. Neural. Eng.*, **2**, S105-S120 (2005).
41. E. Zrenner, Fighting blindness with microelectronics, *Sci. Transl. Med.*, **5**, 1-7 (2013).
42. J. D. Dorn, A. K. Ahuja, A. Caspi, L. da Cruz, G. Dagnelie, J. -A. Sahel, R. J. Greenberg and M. J. McMahon, The detection of motion by blind subjects with the epiretinal 60-electrode (Argus II) retinal prosthesis, *JAMA Ophthalmol.*, **131**, 183-189 (2013).
43. T. T. Kien, T. Maul and A. Bargiela, A review of retinal prosthesis approaches, *Int. J. Mod. Phys.: Conf. Ser.*, **9**, 209-231 (2012).

44. N. L. Wagner, J. A. Greco and R. R. Birge, Visual restoration using microbial rhodopsin, In *Bionanotechnology: Biological Self-Assembly and its Applications*, B. H. A. Rehm, Ed., Caister Academic Press, Norfolk, UK, pp. 205-240 (2013).
45. J.-A. He, L. Samuelson, L. Li, J. Kumar and S. K. Tripathy, Oriented bacteriorhodopsin/polycation multilayers by electrostatic layer-by-layer assembly, *Langmuir*, **14**, 1674-1679 (1998).
46. N. L. Wagner, J. A. Greco, M. J. Ranaghan and R. R. Birge, Directed evolution of bacteriorhodopsin for applications in bioelectronics, *J. R. Soc., Interface*, **10**, 20130197 (2013).
47. D. Oesterhelt and W. Stoeckenius, Functions of a new photoreceptor membrane, *Proc. Natl. Acad. Sci. U.S.A.*, **70**, 2853-2857 (1973).
48. D. Oesterhelt and W. Stoeckenius, Rhodopsin-like protein from the purple membrane of *Halobacterium halobium*, *Nature (London, New Biol.)*, **233**, 149-152 (1971).
49. H. Luecke, B. Schobert, H.-T. Richter, J.-P. Cartailler and J. K. Lanyi, Structure of bacteriorhodopsin at 1.55 Å resolution, *J. Mol. Biol.*, **291**, 899-911 (1999).
50. C. D. Heyes and M. A. El-Sayed, The role of the native lipids and lattice structure in bacteriorhodopsin protein conformation and stability as studied by temperature-dependent fourier transform-infrared spectroscopy, *J. Biol. Chem.*, **277**, 29437-29443 (2002).
51. R. Bogomolni, R. Baker, R. Lozier and W. Stoeckenius, Light-driven proton translocations in *Halobacterium halobium*, *Biochim. Biophys. Acta, Bioenerg.*, **440**, 68-88 (1976).
52. R. R. Birge, N. B. Gillespie, E. W. Izaguirre, A. Kusnetzow, A. F. Lawrence, D. Singh, Q. W. Song, E. Schmidt, J. A. Stuart, S. Seetharaman and K. J. Wise, Biomolecular electronics: Protein-based associative processors and volumetric memories, *J. Phys. Chem. B*, **103**, 10746-10766 (1999).
53. J. Tittor and D. Oesterhelt, The quantum yield of bacteriorhodopsin, *FEBS Lett.*, **263**, 269-273 (1990).
54. R. R. Birge, T. M. Cooper, A. F. Lawrence, M. B. Masthay, C. Vasilakis, C. F. Zhang and R. Zidovetzki, A spectroscopic, photocalorimetric and theoretical investigation of the quantum efficiency of the primary event in bacteriorhodopsin, *J. Am. Chem. Soc.*, **111**, 4063-4074 (1989).
55. M. B. Jackson and J. M. Sturtevant, Phase transitions of the purple membranes of *Halobacterium halobium*, *Biochemistry*, **17**, 911-915 (1978).
56. R. R. Birge, Photophysics and molecular electronic applications of the rhodopsins, *Annu. Rev. Phys. Chem.*, **41**, 683-733 (1990).
57. C. Bräuchle, N. Hampp and D. Oesterhelt, Optical applications of bacteriorhodopsin and its mutated variants, *Adv. Mater.*, **3**, 420-428 (1991).
58. M. J. Ranaghan, S. Shima, L. Ramos, D. S. Poulin, G. Whited, S. Rajasekaran, J. A. Stuart, A. D. Albert and R. R. Birge, Photochemical and thermal stability of green and blue proteorhodopsins: Implications for protein-based bioelectronic devices, *J. Phys. Chem. B*, **114**, 14064-14070 (2010). N. Hampp, Bacteriorhodopsin as a photochromic retinal protein for optical memories, *Chem. Rev.*, **100**, 1755-1776 (2000).
59. N. Hampp, Bacteriorhodopsin as a photochromic retinal protein for optical memories, *Chem. Rev.*, **100**, 1755-1776 (2000).
60. A. Popp, M. Wolperdinger, N. Hampp, C. Bräuchle and D. Oesterhelt, Photochemical conversion of the O-intermediate to 9-cis-retinal-containing products in bacteriorhodopsin films, *Biophys. J.*, **65**, 1449-1459 (1993).
61. N. B. Gillespie, K. J. Wise, L. Ren, J. A. Stuart, D. L. Marcy, J. Hillebrecht, Q. Li, L. Ramos, K. Jordan, S. Fyvie and R. R. Birge, Characterization of the branched-photocycle intermediates P and Q of bacteriorhodopsin, *J. Phys. Chem. B*, **106**, 13352-13361 (2002).
62. Z. Dánshazy and Z. Tokaji, Blue light regeneration of bacteriorhodopsin bleached by continuous light, *FEBS Lett.*, **476**, 171-173 (2000).

63. M. J. Ranaghan, J. A. Greco, N. L. Wagner, R. Grewal, R. Rangarajan, J. F. Kosciielecki, K. J. Wise and R. R. Birge, Photochromic bacteriorhodopsin mutant with high holographic efficiency and enhanced stability via a putative self-repair mechanism, *ACS Appl. Mater. Interfaces*, **6**, 2799-2808 (2014).
64. J. A. Stuart, D. L. Marcy, K. J. Wise and R. R. Birge, Volumetric optical memory based on bacteriorhodopsin, *Synth. Met.*, **127**, 3-15 (2002).
65. J. A. Stuart, J. R. Tallent, E. H. L. Tan and R. R. Birge, Protein-based volumetric memories, *Proc. IEEE Nonvol. Mem. Tech. (INVMTC)*, **6**, 45-51 (1996).
66. J. A. Greco, N. L. Wagner, M. J. Ranaghan, S. Rajasekaran and R. R. Birge, Protein-based optical computing, In *Biomolecular Information Processing: From Logic Systems to Smart Sensors and Actuators*, E. Katz, Ed., Wiley-VCH: Weinheim, Germany, pp. 33-59 (2012).
67. M. Azadmehr, J. P. Abrahamsen and P. Häfliger, *IEEE International Symposium on Circuits and Systems (ISCAS)*, **3**, pp. 2751-2754 (2005).
68. R. F. Peck, S. DasSarma and M. P. Krebs, Homologous gene knockout in the archaeon *Halobacterium salinarum* with *ura3* as a counterselectable marker, *Mol. Microbiol.*, **35**, 667-676 (2000).
69. B. M. Becher and J. Y. Cassim, Improved isolation procedures for the purple membrane of halobacterium halobium, *Prep. Biochem.*, **5**, 161-178 (1975).
70. D. Oesterhelt and W. Stoeckenius, Isolation of the cell membrane of *Halobacterium halobium* and its fractionation into red and purple membrane, *Methods Enzymol.*, **31**, 667-678 (1974).
71. J.-A. He, L. Samuelson, L. Li, J. Kumar and S. K. Tripathy, Photoelectric properties of oriented bacteriorhodopsin / polycation multilayers by electrostatic layer-by-layer assembly, *J. Phys. Chem. B*, **102**, 7067-7072 (1998).
72. J.-A. He, L. Samuelson, L. Li, J. Kumar and S. K. Tripathy, Bacteriorhodopsin thin film assemblies – immobilization, properties, and applications, *Adv. Mater.*, **11**, 435-446 (1999).
73. C. Scholz, Perspectives on: Materials aspects for retinal prostheses, *J. Bioact. Compat. Polym.*, **22**, 539-568 (2007).
74. S. Roll, J. Müller-Nordhorn, T. Keil, H. Scholz, D. Eidt, W. Greiner and S. N. Willich, Dacron® vs. PTFE as bypass materials in peripheral vascular surgery – systematic review and meta-analysis, *BMC Surg.*, **8**, 1-8 (2008).
75. Y. Liu, T. He, H. Song and C. Gao, Layer-by-layer assembly of biomacromolecules on poly(ethylene terephthalate) films and fiber fabrics to promote endothelial cell growth, *J. Biomed. Mat. Res, Part A*, **81A**, 692-704 (2007).
76. Y. Liu, T. He and C. Gao, Surface modification of poly(ethylene terephthalate) via hydrolysis and layer-by-layer assembly of chitosan and chondroitin sulfate to construct cytocompatible layer for human endothelial cells, *Coll. Surf., B*, **46**, 117-126 (2005).
77. M. C. Wyers, M. D. Phaneuf, E. M. Rzcudlo, M. A. Contreras, F. W. LoGerfo and W. C. Quist, *In vivo* assessment of a novel dacron surface with covalently bound recombinant hirudin, *Cardiovasc. Pathol.*, **8**, 153-159 (1999).
78. A. Matsuzawa, Nano-scale CMOS and low voltage analog to digital converter design challenges, *8th International Conference on Solid-State and Integrated Circuit Technology*, pp. 1676-1679 (2006).
79. A. El Gamal, Trends in CMOS image sensor technology and design, *International Electron Devices Meeting*, pp. 805-808 (2002).
80. C. T. Chiang and C. Y. Wu, Implantable neuromorphic vision chips, *Electron. Lett.*, **40**, 361-363 (2004).
81. L. Wentai, K. Vichienchom, M. Clements, S. C. DeMarco, C. Hughes, E. McGucken, M. S. Humayun, E. De Juan, J. D. Weiland and R. J. Greenberg, A neuro-stimulus chip with telemetry unit for retinal prosthetic device, *IEEE J. Solid-State Circuits*, **35**, 1487-1497 (2000).

82. T. Delbrück and C. A. Mead, An electronic photoreceptor sensitive to small changes in intensity, In *Advances in Neural Information Processing Systems 1*, S. T. David, Ed.; Morgan Kaufmann Publishers Inc., pp 720-727 (1989).
83. C. Mead, *Analog VLSI and Neural Systems* (Addison-Wesley, 1989).
84. A. Mortara and E. A. Vittoz, A communication architecture tailored for analog vlsi artificial neural networks: Intrinsic performance and limitations, *IEEE Trans. Neural Networks*, **5**, 459-466 (1994).